Project 076 Improved Open Rotor Noise Prediction Capabilities

Georgia Institute of Technology

Project Lead Investigator

Professor Dimitri N. Mavris (P.I.)
Director, Aerospace Systems Design Laboratory
School of Aerospace Engineering, Georgia Institute of Technology
404-894-1557
dimitri.mavris@ae.gatech.edu

Dr. Jimmy Tai (Co-P.I.)
Division Chief, Propulsion & Energy
Aerospace Systems Design Laboratory
School of Aerospace Engineering, Georgia Institute of Technology
404-894-0197
jimmy.tai@ae.gatech.edu

University Participants

Georgia Institute of Technology

- P.I.s: Dr. Dimitri N. Mavris, Dr. Jimmy Tai
- FAA Award Number: 13-C-AJFE-GIT-078
- Period of Performance: October 1, 2021 to September 30, 2022
- Task:
  - Task 3: Computational aeroacoustics (CAA) case set-up and validation

Project Funding Level

The project funding is $300,000 per year from the FAA. The cost share match amount is $300,000 per year. The sources of matching are cash and in-kind cost-share from our industry partner (GE).

Investigation Team

Dr. Dimitri Mavris, Professor, Georgia Institute of Technology (Georgia Tech) (P.I.)
Dr. Jimmy Tai, Senior Research Engineer, Georgia Tech (Co-P.I.)
Dr. Miguel Walter, Research Engineer II, Georgia Tech
Mr. Brenton Willier, Graduate Student, Georgia Tech
Mr. Grant Stevenson, Graduate Student, Georgia Tech

Project Overview

The contra-rotating open rotor (CROR) system has promising environmental benefits due to its ultra-high bypass ratio and high propulsive efficiency. The reduced fuel burn and emissions of the CROR compared with an equivalent-thrust turbofan make it a viable, economic, and environmentally friendly propulsion alternative to traditional ducted systems. However, in the absence of a noise-conditioning duct, noise penalties may arise from aerodynamic interactions within the CROR system as well as between the system and surrounding installation components such as the engine pylon. If such a system configuration is not optimized, the added effect of flow asymmetry on the aerodynamic interactions could potentially result in severe noise penalties, making the CROR system infeasible for use in the aircraft industry. In the proposed work, the team will perform a sensitivity study on the design parameters of a CROR-pylon configuration. This study will leverage knowledge from past efforts with this type of configuration in order to narrow down the space of design parameters. High-fidelity CAA

analyses will be performed to analyze the effect of each of the chosen parameters on noise. This research is intended to provide both the FAA and industry with key insights necessary for design optimization of the CROR system in the future.

Task 3 - CAA validation

Georgia Institute of Technology

Objectives

The majority of the work in Year 2 was re-directed by FAA supervision toward an extensive validation campaign of numerical simulations against experimental data. Thus, this task is focused on validating predictions from high-fidelity simulations against available experimental data from an open rotor configuration in order to evaluate discrepancies between numerical simulations and experiments. These efforts will provide evidence of the adequacy of the numerical approach for open rotor design.

Research Approach

The validation approach consists of two parts. The first part is concerned with aerodynamic calibration of simulations against experimental values for an F31/A31 open rotor. Under low Mach conditions, loading noise is the most relevant component. Therefore, loading is enforced by matching the time-averaged thrust. The calibration process results in blade pitch settings that minimize discrepancies between experimental and simulated thrusts. The second part concerns acoustic validation of the F31/A31 open rotor, which is achieved by employing calibrated pitch settings.

A hybrid approach for CAA is adopted in this work. High-fidelity simulations are the focal point of the study, and thus, such simulations are employed. The unsteady aerodynamic flow-field is simulated using a lattice Boltzmann method (LBM) solver, while far-field aeroacoustics are predicted by a Ffowcs Williams–Hawkings (FW-H) solver.

Methodology

Validation cases and experimental data

This study employs data from NASA experiments (Elliott, 2011; Sree, 2015; Stephens, 2014) or a wind tunnel open rotor model based on GE design F31/A31 blades. The validation cases are those from low-regime F31/A31 experiments, specifically for the nominal take-off (NTO) pitch setting and without the pylon geometry. The experimental NTO cases (Sree, 2015; Stephens, 2014) as a function of varying operational parameters are illustrated in Figure 1, shown as gray symbols, along with the cases chosen for validation, shown as red and blue symbols. The validation cases are chosen at rotor speeds spanning the upper half range (RPMc = 5,550.5–6,432.0). The experimental data used in the current study come from two sources: a) NASA experiments on the F31/A31 open rotor geometry and b) GE Aerospace data on the same F31/A31 experiments. The former source of data is exclusively employed for acoustic validations, while the latter is for aerodynamic calibration and comparisons. These data were shared by GE Aerospace as an industrial partner in the FAA ASCENT A76 project and are proprietary; consequently, the data are not shown here.

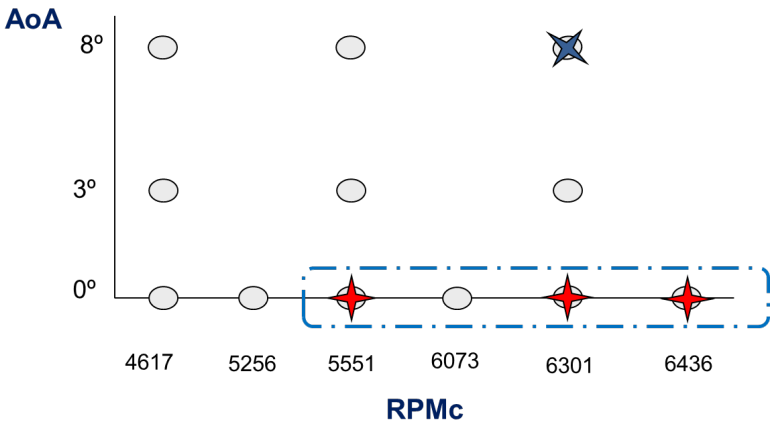

Figure 1. Validation cases as function of and corrected rotor speed (RPMc) and angle of attack (AoA)

The team employed acoustic data from NASA experiments for F31/A31(Elliott, 2011; Sree, 2015; Stephens, 2014). Three data sets are provided in the supplemental information of the NASA report (Stephens, 2014) in the form of power spectral density (PSD). These data sets are described in Table 1.

Table 1. Description of NASA acoustic data.

Data Set	Description	Remark
11	As-measured spectral data	
21	Microphone-corrected spectra	Includes corrections due to microphone and bullet-nose sensitivity and directivity
41	1-ft lossless spectra	Losses due to atmospheric attenuation are restored as gains

From the above data sets, set 41 includes all of the needed corrections, except for wind tunnel background corrections. Therefore, the fully corrected data are based on data set 41. This data set is then corrected for the background wind tunnel based on RDG 802 (set 41), which contains spectral data for the wind tunnel and model without blades (Stephens, 2014). The procedure for obtaining the fully corrected data set is as follows:

- Set 41 is converted to the sound pressure level (SPL) from PSD:

$$SPL = PSD + 10\,log_{10}(\Delta f)$$

- Set 41 in SPL is scaled back to the sideline location.
- Fully corrected data are obtained by removing the wind background noise:

$$SPL^{*} = 10\,log_{10}\left[10^{SPL/10} - 10^{SPL_{WT}}\right]$$

Two additional corrections (Rizzi, 2016) are introduced:

- The first correction ensures that the wind tunnel background does not exceed the microphone SPL to avoid invalidating the above calculation.

- The second correction rectifies low-frequency noise associated with the wind tunnel. Below 700 Hz, noise is removed by replacing that portion of data with a parabolic function with 10-dB attenuation, relative to the 700-Hz level, at 100 Hz.

Calibration in aerodynamics

Aerodynamic calibration is considered prior to acoustic validation. For low Mach conditions, loading noise is the most relevant component. Because this type of noise is thrust-dependent, enforcing a loading equality constraint is viewed as a necessary requirement for acoustic validation. Here, loading is enforced by matching the time-averaged thrust. However, it is acknowledged that this time-averaged measure might not be sufficient, as other factors may also play a role. Note that there is no attempt to directly bring CAA predictions close to experimental values; rather, CAA predictions are evaluated given that a loading metric has been met.

Pitch settings for thrust matching are calibrated by minimizing a cost function, L, consisting of the thrust discrepancy between simulations and experiments according to the following equation:

$$\boldsymbol{\zeta}^* = arg_{\zeta} \min L$$

The cost function, $L = \| \boldsymbol{w}^t \ \boldsymbol{\Delta} \|_2$, is an equally weighted l-2 norm measure of individual rotor discrepancy between the simulation thrust prediction T^{sim} and experimental thrust T^{exp}:

$$\Delta = \begin{bmatrix} \left(T_f^{sim}(\zeta) - T_f^{exp} \right) / T_f^{exp} \\ \left(T_a^{sim}(\zeta) - T_a^{exp} \right) / T_a^{exp} \end{bmatrix}$$

The calibration parameters, $\zeta = [\beta_f, \beta_a]$, contain the pitch angles of the forward and aft rotors. Such parameters vary around the nominal pitch setting:

$$[\ \beta_f^n, \beta_a^n\ ] = [\ 40.1\ °, 40.8°\ ]$$

The simulation values used to calculate discrepancies are approximated via linear regression models, fitted from training data stemming from LBM simulations. These training data consist of the forward and aft thrust from simulations for different pitch settings, which are varied around the nominal pitch setting. Note that the employed linear models are considered appropriate, as departures from the nominal pitch settings are expected to be small. A total of eighteen simulations (six per calibration case, RPMc = 4,620.0; 5,550.5; 6,432.0) were carried out. Simulations were conducted with discretization sizes of approximately 160 million voxels. Note that the resulting resolution is coarser than that used for aeroacoustics predictions; however, it is considered a suitable compromise between computational cost and accuracy based on resolution studies, which show variation within only 1% in thrust predictions between simulations at different resolutions.

Validation in acoustics

Acoustic validations are performed using the calibrated pitch blade settings obtained via the above procedure. An additional validation case at the nominal pitch setting is included as well in order to compare the numerical prediction against the calibrated case. This additional validation case is chosen at the lowest rotor speed among the considered cases, as shown in Figure 1. This case will also serve as a reference to highlight the effects of calibration on the acoustical results. The remaining validation cases for the calibrated parameters are performed next.

The rotor speed range in the present acoustic validations targets the upper half of the rotor speed span of the F31/A31 experiments. International Civil Aviation Organization certification limits the effective perceived noise level – a human-hearing-weighted and time-averaged metric of overall sound level - of each aircraft. This process examines three flight conditions (takeoff, flyover, and approach) and compares the resulting effective perceived noise level against a maximum value. Because the takeoff and flyover flight regimes are dominated by engine noise, as opposed to approach and airframe noise, these flight rotor speeds will continue to be the focus of this study. The calibration and validation cases addressed in the current study are a subset of the NASA experiments (Elliott, 2011; Sree, 2015) at the NTO pitch settings, as shown in Figure 1.

The frequency range is an important aspect to consider in this study. The ideal frequency range to be addressed in the current study should cover the entire high-annoyance portion (i.e., human-hearing constraint) at 10 kHz. This value applies to the full-scale model, whereas in the wind tunnel model, this threshold increases to 50 kHz, based on a scale factor of 5 with respect to the full-scale model (Stephens, 2014). Simulations in the current study attempt to address at least part of the high-annoyance portion. Consequently, most overall noise metrics will be computed in the range of 0.5–50 kHz for consistency with experiments.

Numerical Simulations

Simulations in the current study rely on a hybrid strategy for CAA analysis. The unsteady aerodynamics flow-field is simulated by means of an LBM solver. During the runtime of the aerodynamic solver, flow-field data are collected at specified surfaces. These data are then used as input to a far-field acoustics solver. An acoustic solver based on the FW-H equations is then employed for predicting far-field acoustics. Both aerodynamics and acoustics methods are described in more detail below.

Geometry employed in simulations
The geometry of interest is an open rotor based on the sub-scale model corresponding to the GE design F31/A31 blade set. The geometry details are provided in Table 2:

Table 2. Sub-scale F31/A31 open rotor.

	Number and type of blades	Diameter
Front rotor	12 / F31	0.66 m
Aft rotor	10 / A31	0.63 m

The geometry includes the nacelle as well as the rotating hub for both front and aft rotors. Nevertheless, the simulated geometry does not include the blade-to-blade angle variation from assembly present in the experiment (Sree, 2015), as such information is not available. The geometry in the simulations also differs from the actual experiment in that the aft extension of the nacelle downstream of the aft rotor is purely cylindrical instead having a varying sectional radius as in the actual geometry. Moreover, the geometry used in our simulations does not include gaps in junctions such as those found between the nacelle and rotating hubs and between the blades and hubs.

The utilized F31/A31 blade shape corresponds to the maximum-climb flight condition. The geometry was provided with blade pitch settings of 60.5°/59.0°. Thus, any blade pitch setting addressed in the current study is determined from the aforementioned forward and aft pitch angles. Moreover, the blade shapes are fixed according to the maximum-climb flight condition regardless of the operational parameters of the simulated cases. As previously reported (Falissard, 2018), blade deformations due to the operating point influence aerodynamics and acoustics performance. The balance between aerodynamic, centrifugal, and Coriolis forces results in blade deformation, especially on the outward half span of the blades. Larger deformations are observed for the cruise condition, followed by the take-off and approach conditions. Differences in shape between non-running and running blades exhibited differences of approximately 5% in thrust coefficient predictions. Thus, the study found that accounting for blade deformations improves simulation predictions. Ideally, each operating condition in the simulations should use the corresponding deflected shape. Unfortunately, a lack of information on blade shapes prevented accounting for such effects. Therefore, the only available shape (i.e., at maximum climb) is employed in the present study.

Unsteady aerodynamics
The unsteady aerodynamic flow-field is obtained by employing a commercial LBM solver, PowerFLOW. Unlike traditional fluid mechanics solvers, which are based on a continuity assumption via the Navier–Stokes equations and solve for macroscopic quantities, the LBM solves for the Boltzmann equations by tracking the evolution of microscopic particle distributions in the fluid. Thus, modeling occurs at a mesoscopic scale, corresponding to simplified microscopic behavior, where the physics are more fundamental. Such modeling results in low dispersion and dissipation properties, which is highly desirable for aeroacoustics purposes.

Turbulence modeling is achieved by means of a very large eddy simulation. To reduce the spatial resolution requirement in near-wall regions, a hybrid wall treatment model is chosen. This modeling is based on the standard log law of the wall and includes a laminar sub-layer model accounting for the effects of favorable and adverse pressure gradients.

The boundary conditions are defined as follows: in the outer boundaries, pressure/velocity boundary conditions are prescribed, whereas non-slip wall boundary conditions are prescribed on surfaces of both rotors and the nacelle. In the nacelle extension, however, slip wall boundary conditions are prescribed in order to avoid the influence of boundary layers in those locations. The boundary values ($V_\infty, T_\infty, p_\infty$) and rotor speed in the current simulations are set to those of the wind tunnel conditions and rotor speed measured in the F31/A31 experiments, ,respectively; however, their values are not provided here owing to proprietary restrictions.

Spatial discretization is achieved via variable refinement (VR) regions. The spatial resolution increases two-fold with each VR level. The highest resolution is used at the leading and trailing edges of the blades, whereas the second highest resolution is applied at the tip of the blades, specifically in the volumetric regions at the tips, in order to resolve the tip vortex. Details regarding the employed VR levels are shown in Table 1. The highest resolution is 0.125 mm, whereas the solver time step is approximately 3.7×10^{-7} s. The typical discretization size for simulations in the current study is approximately 900 million voxels. This size is the upper limit that can be computationally afforded in the current study,

Table 3. Lattice Boltzmann method (LBM) simulation set-up. LE: leading edge; TE: trailing edge.

LBM Simulation	***Value***	***Remark***
Smallest spatial discretization	0.125 mm	At blade LE, TE, and tips
Time step	0.370 μs	
Mesh size	900 million voxels	Typical discretization

Aeroacoustics

The far-field aeroacoustics are predicted by employing a commercial FW-H solver, PowerAcoustics. Moreover, to prevent acoustic reflections from the outer boundaries, a sponge region surrounding the open rotor geometry toward the outer boundaries is considered. In this region, the fluid kinematic viscosity is progressively increased so that outgoing acoustic waves are dissipated.

As input, the FW-H solver takes flow data collected at certain surfaces. These surfaces can be either permeable or impermeable. Employing permeable FW-H surfaces for addressing, even partially, the high-annoyance portion of noise spectra would require such a high spatial resolution that the simulations would be intractable for the current study. Thus, impermeable FW-H surfaces are employed instead. These surfaces are defined at both rotor surfaces, including not only the blades but also the rotating hub part.

Flow data are recorded at the aforementioned impermeable FW-H surfaces for collection time periods of 12–16 rotor revolutions at a rate of approximately 190 kHz. Spectral data are obtained by applying a Fourier transformation to the resulting data from the acoustic solver. The employed window width is 50%, and a parabolic Welch windowing function with 50% overlapping is applied to the acoustic data.

Acoustical data are obtained at the sideline receivers as described for previous experiments (Sree, 2015); these receivers are located at a distance, d, of 5 ft from the rotor. This set consists of 18 receivers, spanning from approximately 17.5 ^{o} to 140^{o}, and is uniquely used for calculating discrepancy measures for comparison with experimental results. Likewise, a second set is also defined, consisting of sideline receivers located at the same distance d, but with a higher spatial resolution of 2.5^{o} separation and spanning a larger range of angles, 15 ^{o}–160 ^{o}. The receiver arrangement is illustrated in Figure 2.

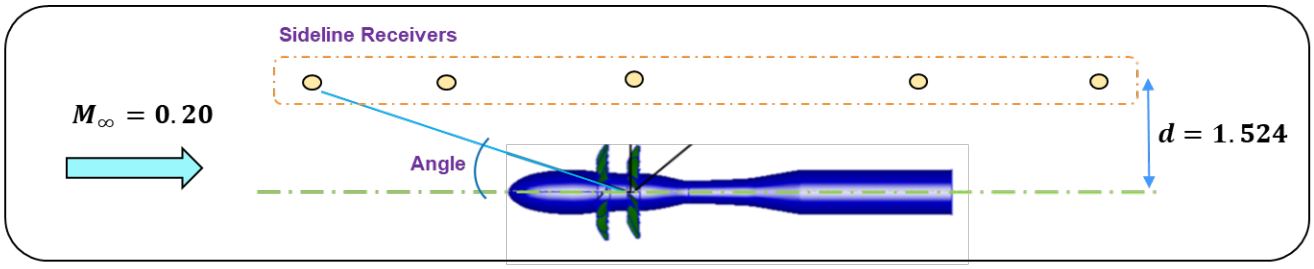

Figure 2. Receiver arrangement for the F31/A31 experiments (figure adapted from Nark et al. [6]).

Results

Calibration in aerodynamics

Results from the aerodynamics calibration are shown in Table 4 as angular departures ($\delta\beta$) from the NTO pitch setting, such that $\beta^* = \beta^n + \delta\beta^*$, where β^n is the NTO angle. Note that for all rotor speeds investigated in this study, the resulting pitch angles increase slightly over the nominal angle due to thrust underprediction at the nominal angles. Moreover, after calibration, the aerodynamics are re-calculated at higher-resolution LBM simulations, which is needed for aeroacoustics. Hence, the resulting thrust may vary slightly; however, the discrepancy for each individual rotor is within 1%, which is in accordance with the experimental uncertainty (Stephens, 2014). In addition, the calibrated pitch at RPMc = 6,250.5 is taken to be the same as that for the highest rotor speed because the predicted thrust is found within the acceptable threshold for calibration, which is verified by the calculated thrust discrepancy, as shown in Figure 3 (right).

Table 4. Resulting calibrated pitch setting.

RPMc	$\delta\beta_f^*$	$\delta\beta_a^*$	*Remark*
5,550.5	+ 0.288°	+ 0.709°	
6,250.5	+ 0.460°	+ 0.428°	Same as that for the highest rotor speed
6,432.0	+ 0.460°	+ 0.428°	

Comparisons of thrust between LBM predictions, previous simulations (Nark, 2016) and experimental measurements are shown in Figure 3. All solvers can well predict thrust trends with rotor speed, as shown on the left; however, for the nominal pitch setting, all of the solvers exhibit some degree of discrepancy from experimental measurements, as shown on the right. LBM simulations for the calibrated pitch setting exhibit the smallest discrepancy due to the thrust-matching process. At nominal pitch settings, there are apparent variations in predictions among solvers: corresponding LBM simulations underpredict the thrust at all rotor speeds, whereas predictions from a previous study (Nark, 2016) mostly overpredict the thrust. Discrepancy levels are smaller for the OVERFLOW solver, whereas the FUN3D solver and LBM simulations exhibit comparable magnitudes of discrepancy.

Torque ratio predictions from LBM simulations and previous studies (Nark, 2016) are compared with NASA experimental results in Figure 4. For the nominal pitch setting, none of the solvers accurately capture the trends, as shown on the left. Indeed, all solvers predict monotonically decreasing trends with rotor speed, while the NASA experiments exhibit a nearly flat trend. In contrast, the LBM simulations with calibrated pitch settings produce not only qualitatively better trends but also closer values. Discrepancies in torque ratio, shown on the right, exhibit a significant departure from the experimental results at the lowest rotor speed for all simulations with the nominal pitch setting; however, these discrepancies decrease with increasing rotor speed.

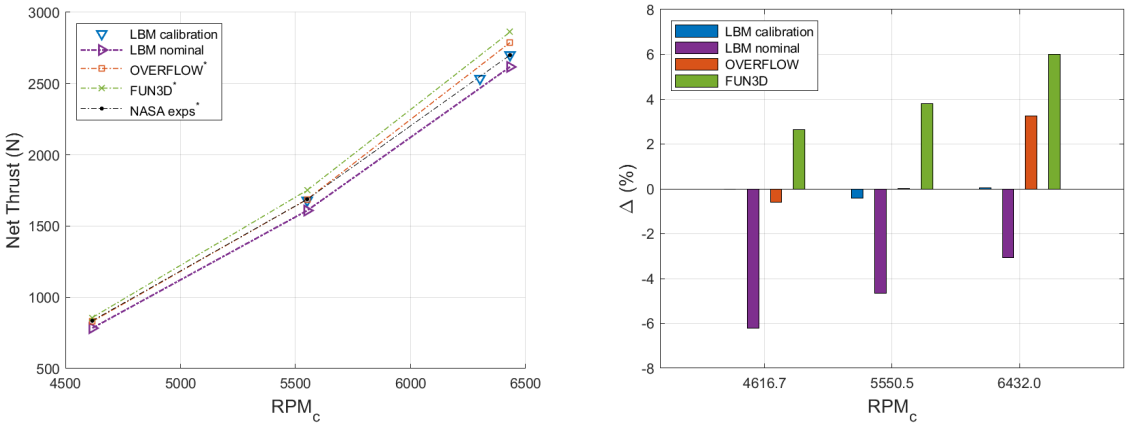

Figure 3. Thrust comparison: simulated and experimental thrust (left) and discrepancy with experimental results (right). LBM: lattice Boltzmann method.

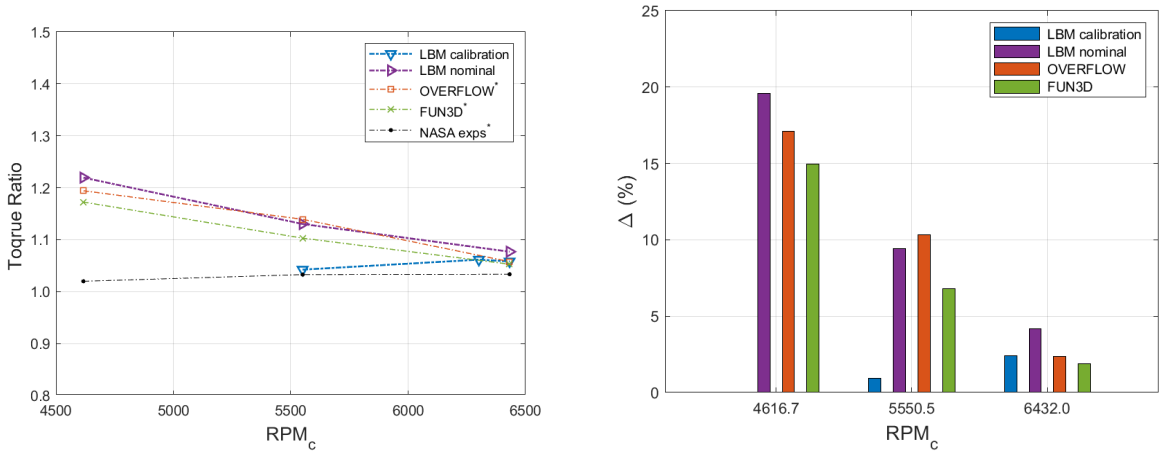

Figure 4. Torque ratio comparison: simulated and experimental torque ratio (left) and discrepancy with experimental results (right). LBM: lattice Boltzmann method.

Validation in acoustics

The effect of calibrating pitch settings on overall noise metrics is shown in Figure 5. Overall SPL (OASPL) directivities from simulations using both calibrated and nominal pitch settings along with that of NASA experiments are shown on the left, while respective average discrepancies are shown on the right. The predictions are from intermediate-resolution simulations of approximately 600 million voxels. There is a notable variation in agreement between simulations and experiments along directivity angles. Small differences are found for intermediate angles of 25°–80°, whereas the differences increase for smaller and larger forward and aft angles, respectively. Moreover, no observable differences in directivity were found between predictions for the nominal and calibrated pitch settings. Indeed, in terms of overall noise metrics, small changes in discrepancy were found between the calibrated and nominal pitch settings, at 0.05 dB for OASPL and 0.29 dB for the overall power level (OPWL).

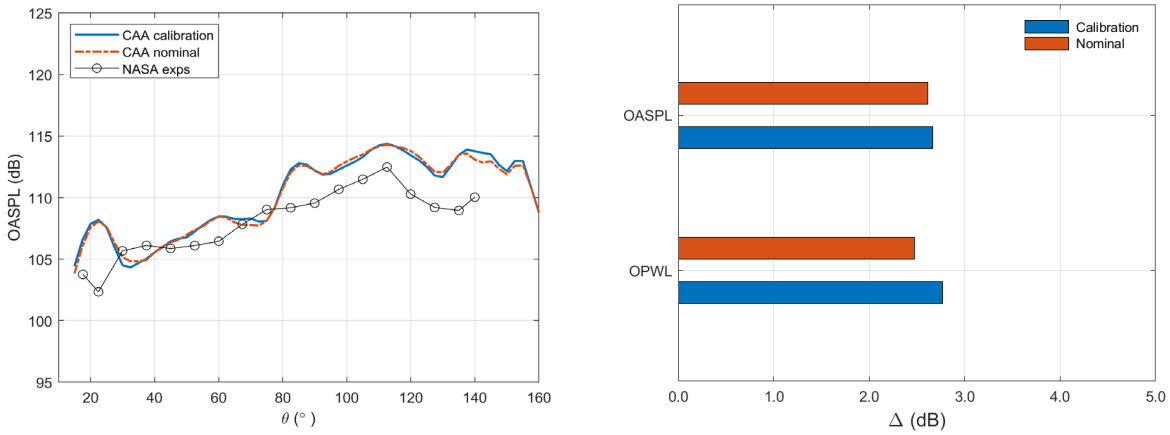

Figure 5. Comparison between nominal and calibrated pitch settings: OASPL directivity (left) and discrepancy (right). CAA: computational aeroacoustics; OASPL: overall sound pressure level; OWPL: overall power level.

The OASPL directivity for different rotor speeds and the corresponding averaged discrepancies for all calibrated pitch settings are shown in Figures 6 and 7. The OASPL associated with the directivity curves clearly increases with increasing rotor speed, as expected. Note that small changes in OASPL values are observed at most directivity angles for the two highest rotor speeds due to their proximity in RPMc. Moreover, a closer agreement in trends and values can be seen for the two highest rotor speeds, especially for directivity angles of 20°–100°. To illustrate the effect of different corrections in the experimental measurements, discrepancies are calculated with respect to all relevant sets of the experimental data, as previously described. Note that partial correction in experimental data could lead to discrepancy variations of 0.2–0.5 dB. Nevertheless, the actual discrepancy is measured with respect to the fully corrected data (blue bar). Values of approximately 1.5 dB are found for the two highest rotor speeds, whereas the discrepancy is larger for the lowest rotor speed, at approximately 2.5 dB.

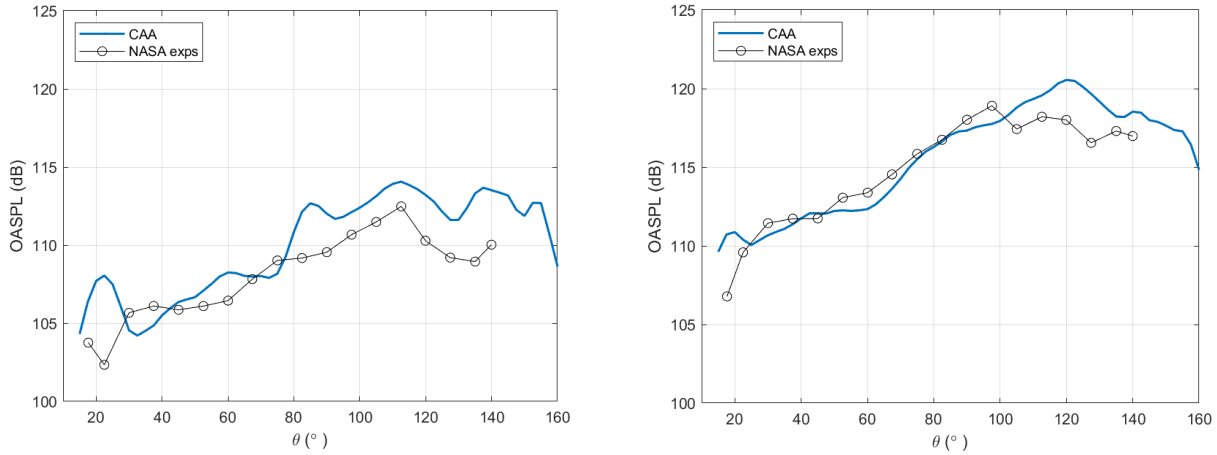

Figure 6. OASPL directivity: 5,550.5 RPMc (left) and 6,301.4 RPMc (right). CAA: computational aeroacoustics; OASPL: overall sound pressure level.

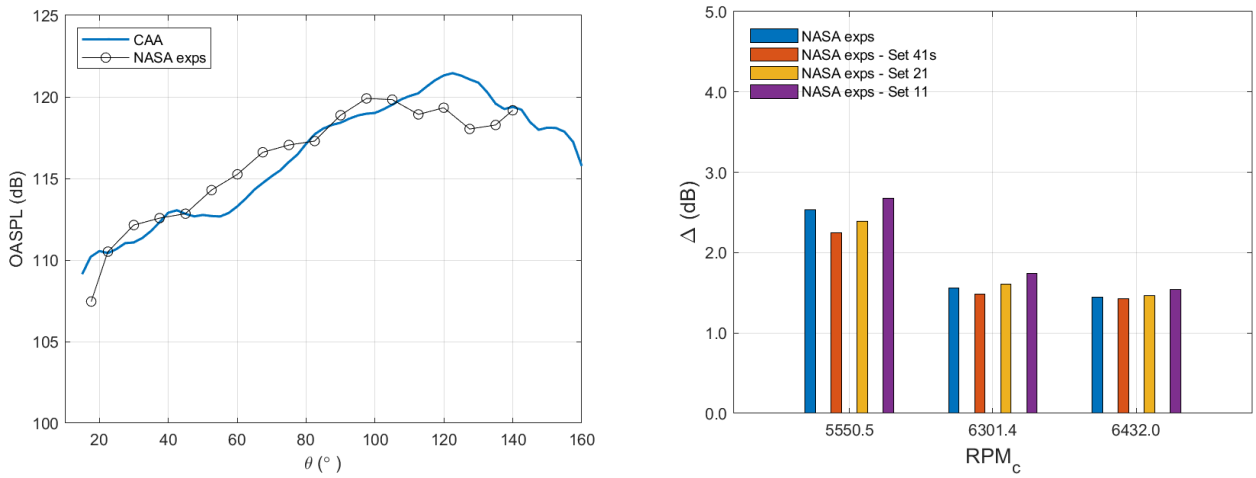

Figure 7. OASPL directivity at 6,432 RPMc (left) and discrepancy (right). CAA: computational aeroacoustics.

Acoustic energy generated by the open fan configuration is calculated from the OPWL. This quantity is calculated by integrating the source power level spectrum for frequencies from 0.5 to 50 kHz. The power level spectrum is obtained by assuming axisymmetry with respect to the propulsor axis, $\psi \in [0, 2\pi]$, and is calculated by using only the same receiver locations used in the experiments. The sideline acoustics data are mapped onto a constant radius, equal to the sideline distance *d*, by assuming spherical spreading (Stephens, 2014). Comparisons of OPWL calculated from simulations and that of experiments are shown in Figure 8. The OPWL trends with corrected rotor speed are in qualitative agreement with the experimental trends, as shown on the left. Closer agreement is found above 6,000 RPMc, whereas the agreement decreases at lower speeds. Numerical predictions are closer to the experimental values at the two highest rotor speeds, with an average discrepancy of less than 1 dB, whereas larger values of 2.5 dB are found at the lowest rotor speed, as shown on the right.

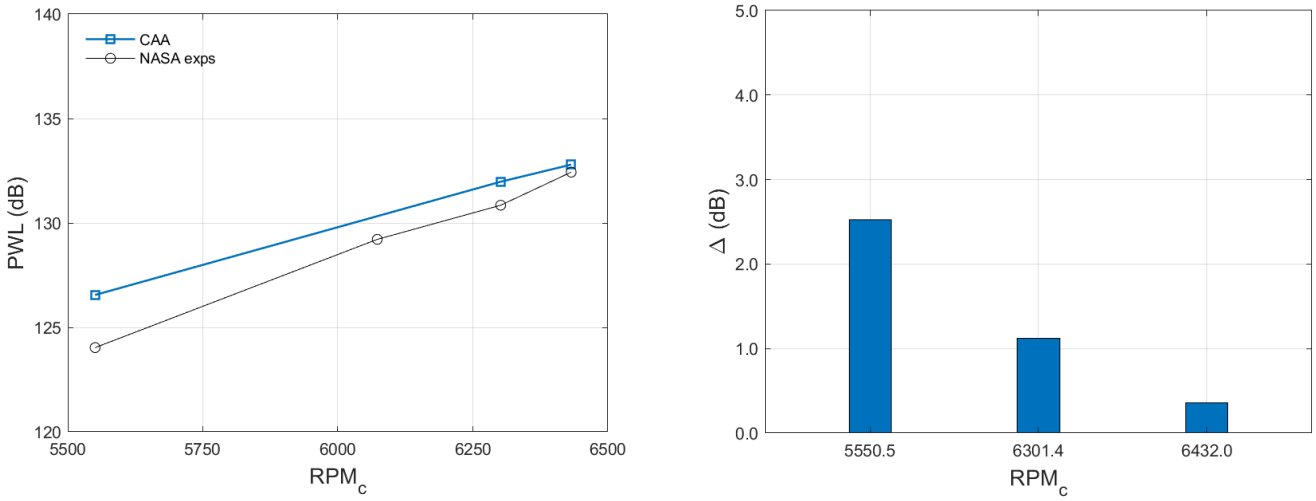

Figure 8. Overall power level (PWL) for calibrated cases. CAA: computational aeroacoustics.

Considerations

The results reported in this document should be viewed in light of the following considerations:

1. Lack of knowledge regarding actual geometry

- Variability in installation of the F31/A31 wind tunnel model, such as blade pitch variation, could lead to angular variations of up to 0.1° from blade to blade.
- Blade deformation may arise from rotation, as blades deform differently at each rotor speed.

2. Simulation aspects
   - The FW-H solver with impermeable surfaces does not account for convection effects (Cerizza, 2022).
   - Impermeable surfaces may not account for very near effects in the flow-field.

Note that each of the above considerations can influence the simulation predictions and hence may result in discrepancies, although the magnitude of these discrepancies is unknown. Installation variability has been argued to result in discrepancies in both aerodynamics and acoustics (Nark, 2016; Envia, 2012). Moreover, neglecting deformations due to operating conditions has also been found to result in aerodynamic and acoustic discrepancies (Falissard, 2018).

Aspects related to simulations are currently being addressed by the authors and will be reported in future work. However, aspects related to a lack of knowledge in geometry are intrinsic to experiments and thus unavoidable in simulations unless provided as part of the outcome from experiments.

Milestones
None.

Major Accomplishments
Extended validation has been completed for all cases at a zero angle of attack.

Publications
"Aerodynamic Calibration for Aeroacoustics Validation of an Open Fan Configuration," to appear on AIAA SciTech 2023.

Outreach Efforts
None.

Awards
None.

Student Involvement
For this task, Brenton Willier (continuing PhD student) and Grant Stevenson (continuing MS student) worked on geometry preparation for numerical analysis and acoustic data analysis.

Plans for Next Period
Future work will focus on completing the remaining validation cases. These remaining cases include a case with a non-zero angle of attack and a case with the nominal pitch setting.

References
Elliott, D. (2011, June 5). Initial investigation of the acoustics of a counter rotating open rotor model with historical baseline blades in a low-speed wind tunnel. *17th AIAA/CEAS Aeroacoustics Conference (32nd AIAA Aeroacoustics Conference)*. 17th AIAA/CEAS Aeroacoustics Conference (32nd AIAA Aeroacoustics Conference), Portland, Oregon. https://doi.org/10.2514/6.2011-2760

Sree, D. (2015). *Far-field acoustic power level and performance analyses of F31/A31 open rotor model at simulated scaled takeoff, nominal takeoff, and approach conditions* (Report No. 2015-218716). NASA. https://ntrs.nasa.gov/citations/20150008245

Stephens, D. B. (2014). *Data Summary Report for the Open Rotor Propulsion Rig Equipped with F31/A31 Rotor Blades* (Report No. 2014-216676). NASA .

Rizzi, S. A., Stephens, D. B., Berton, J. J., Van Zante, D. E., Wojno, J. P., & Goerig, T. W. (2016). Auralization of flyover noise from open-rotor engines using model-scale test data. *Journal of Aircraft*, *53*(1), 117–128. https://doi.org/10.2514/1.C033223

Falissard, F., Chelius, A., Boisard, R., Gaveriaux, R., Canard-Caruana, S., Delattre, G., Gardarein, P., & Mauffrey, Y. (2017, June 5). Influence of blade deformations on open-rotor low-speed and high-speed aerodynamics and aeroacoustics. *23rd AIAA/CEAS Aeroacoustics Conference*. 23rd AIAA/CEAS Aeroacoustics Conference, Denver, Colorado. https://doi.org/10.2514/6.2017-3869

Nark, D. M., Jones, W., Boyd, D., & Zawodny, N. (2016, January 4). Isolated open rotor noise prediction assessment using the F31A31 historical blade set. *54th AIAA Aerospace Sciences Meeting*. 54th AIAA Aerospace Sciences Meeting, San Diego, California, USA. https://doi.org/10.2514/6.2016-1271

Envia, E. (2012). *Open Rotor Aeroacoustic Modeling* (Report No. 2012-217740). NASA.

Cerizza, D. (2022). *DS Simulia corporation*. Private Communication.